Orientation of Channel Die-Compressed
Ultra-high Molecular Weight Polyethylene

by

Yot Boontongkong

B.S., Materials Science and Engineering
Northwestern University, 1995

Submitted to the Department of Materials Science and Engineering
in Partial Fulfillment of the Requirements for the Degree of

Master of Science in Materials Science and Engineering

at the
Massachusetts Institute of Technology
June, 1997

Signature of Author ....
Department of Materials Science and Engineering
May 9, 1997

Certified by ....
Robert E. Cohen
St.Laurent Professor of Chemical Engineering
Thesis Supervisor

Accepted by ....
Michael F. Rubner
TDK Professor of Polymer Materials Science and Engineering
Thesis Reader

Accepted by ....
Linn W. Hobbs
John F. Elliott Professor of Materials
Chairman, Department Committee on Graduate Students
Science

Orientation of Channel Die-Compressed Ultra-high Molecular Weight Polyethylene

by

Yot Boontongkong

Abstract

Ultra-high molecular weight polyethylene (UH) samples were compressed using a channel die and characterized by wide-angle and small-angle X-ray scattering. The experimental results were compared to previous studies performed on high density polyethylene (HDPE).

Most deformation mechanisms exhibited by UH were also observed in HDPE. The onset of crystallographic and morphological texturing occurred at lower compression ratios in UH than in HDPE. Greater resistance to deformation and more extensive strain recovery were also exhibited by UH. These behaviors were attributed to the larger number of tie molecules and higher degree of entanglement within the amorphous region of UH - a direct effect of its high molecular weight.

We have shown that crystallographic texturing in UH, especially molecular orientation along the flow direction, can be controlled by channel die compression. This renders the method suitable for production of oriented samples for future studies of the relation between crystallographic texture and wear behavior.

Thesis Supervisor: Robert E. Cohen

Title: Professor of Chemical Engineering

Acknowledgments

I would like to thank professor Cohen for always being positive, supportive and enthusiastic about my work, and for being great teacher and thinker. It has been my privilege to have been a part of his classes and his group.

Thank to Dr. Anuj Bellare for his expertise and for overseeing the work from the start to the finish - a good deal of credit to him.

Thank to Dr. Zbignew Bartczak for his generous inputs from his vast knowledge on the subject matter.

Thank to everyone in the Cohen group who have helped me in getting around the lab, particularly to Jane Ciebien for her positive and lively attitude, and for making our lab a fun place to be in.

Thank to all my PPST classmates for working together on our classes and for our cooperative effort on the quals! I am glad to have been a part of our class.
A special thank to Ken Lau for his wisdom and kind help.

A sincere thank to Fern. Alvarez, whose pep talks have helped me finished this thesis in time. Finally, I would like to thank those friends whom I have met over the past two years. Their impressive minds have made this institute a very special place.

Table of contents

List of Figures

List of Tables

List of Abbreviations

UH	Ultra-high Molecular Weight Polyethylene
HDPE	High Density Polyethylene
CD	Constraint Direction
FD	Flow Direction
LD	Load Direction
a-pfg	Pole Figure of the a-axes
b-pfg	Pole Figure of the b-axes
c-pfg	Pole Figure of the c-axes
SAXS	Small-angle X-ray Scattering
CMSE	Center for Materials Science and Engineering
Brkhvn	Brookhaven National Synchrotron Light Source
2D	Two-dimensional
1D	One-dimensional
λ	Compression Ratio

1. Introduction

1.1 Motivations

Ultra-high molecular weight polyethylene (UH) is currently used as a bearing surface in total joint replacement prostheses - as acetabular cups in the hip joint and as tibial and patellar components in the knee joint. Though a tough, low friction thermoplastic, prolonged functioning inside a patient's body produces wear debris that stimulates biological response to eliminate the debris. Unfortunately, such response often results instead in loss of bone, leading to loosening of the prosthesis and other complications.

Such undesirable effects provide a driving force to improve the wear performance of UH. The material currently used for artificial joints undergoes no processing to specifically maximize wear performance. We believe that molecular orientation affects the wear behavior of UH, and that the wear properties could be optimized with an appropriate processing method. Certainly, a better knowledge of the relationship between wear properties and the material structure is necessary.

One of our goals has been to establish a controlled texturing method for UH and characterization of the oriented polymer. A previous study [1] showed that channel die compression induced quasi-single crystallographic texture in high density polyethylene (HDPE). Therefore, we chose channel die compression as the method to induce texture in UH. We believe that the wear test results of our textured material, performed in the MIT Tribology Group, will lead to a better design of UH components for the biomedical application.

Superior toughness and wear property of UH [2] among various thermoplastics - HDPE in particular - are attributed to its structure, which is a direct effect of its high molecular weight. Briefly, the increased molecular weight retards the ability of chains to reptate upon melt crystallization, resulting in higher number of tie molecules and higher degree of entanglement within the amorphous region; hence, the enhanced mechanical properties.

Another motivation for our study derived from the existing knowledge of deformation-induced texture development of HDPE. Extensive studies of HDPE deformation have been performed by our research group, particularly under plane strain compression [1]. UH is the higher molecular weight version of polyethylene, rendering itself a suitable material for an extension of the previous studies. In addition, previous detailed analyses from the deformation process of HDPE would provide the basis for comparison and contrast to our UH plane strain compression results.

1.2 Background on HDPE Studies

1.2.1 Literature review of HDPE deformation

Deformation-induced texturing to enhance mechanical properties of HDPE has been used for a variety of applications such as fiber and film drawing. The impact of its application has provided the driving force for a number of experimental studies on HDPE under various deformation modes: uniaxial tension and compression, simple shearing, rolling, and plane-strain compression. The mechanisms underlying plastic deformation of semicrystalline polymers have been reviewed by Bowden and Young [3].

In particular, many early studies were conducted using uniaxial tensile deformation. It was proposed by Peterlin [4] that a catastrophic event in the deformation process called micro-necking, a microscopic cavitation process required to accommodate large strain, was responsible for unraveling and reformation of lamellae.

Experiments using rolling [5] and channel die compression [1,6] modes presented contradictory evidence that large-strain restructuring and molecular alignment could be obtained without a catastrophic reconstruction process. Galeski et al. [1] concluded that a systematic mechanism in which of a series of crystallographic deformation mechanisms occurred, followed by pinching-off of stretched lamellae interface and interface migration, was responsible for the continuous, volume-preserving transformation at large strain.

Though not as extensively as experimental studies, computational studies on HDPE deformation have been performed. Argon et al. [7] developed computational

models to simulate stress-strain responses and texture evolution of uniaxially-compressed and channel die-compressed HDPE. Comparison with the associated experimental results of uniaxial compression [8], where there was no restructuring of interlamellar long period, yielded good agreement. Texture evolution of channel die compression agreed with the simulated results up to a certain degree of deformation: the simulated results did not incorporate the morphological transformation observed at large strain.

1.2.2 Channel Die compression of HDPE

Plastic deformation of crystalline lamellae occurs via a number of mechanisms: crystallographic slip, twinning, and stress-induced martensitic transformation. A quasi-single crystal of HDPE obtained from plane-strain compression was used as a macroscopic approximation to a single crystal to probe deformation resistance of specific crystallographic plastic deformation mechanisms [9]. The study showed that competition among crystallographic deformation mechanisms exists. Individual crystalline deformation mechanisms were isolated and examined. The least resistant slip mechanism was determined to be the (100)[001] chain slip with a critical resolved shear stress of 7.2MPa. The (100)[010] transverse and (010)[001] chain slips have CRSS values of 12.2 and 15.6MPa, respectively. Other slip mechanisms, twinning, and martensitic transformation may be also be active, but only to a very small extent even at large deformation.

According to the extensive channel die compression study by Galeski et al. [1], it was determined that interlamellar sliding - deformation of the amorphous component and the easiest deformation mechanism to initiate - was prominent only at low compression ratios. After this amorphous sliding 'locked' as molecular extension of tie molecules was exhausted, intense activity by the (100)[001] chain slip was observed. This was followed by activation of (100)[010] transverse slip. The dominant (100)[001] slip and the (100)[010] slip, working in cooperation with each other, eventually resulted in a monocrystal texture at high compression ratio of 6.4. No other crystallographic deformation mechanisms were activated, except possibly (110) twinning towards the highest compression ratio of 12, where a trace of fibrillar texture was observed.

Due to both crystallographic and amorphous deformation mechanisms, normals to the originally randomly distributed lamellae were found to rotate towards the loading direction as the lamellae thinned down and stretched out. At the compression ratio of 3.13, the transformation in the lamellar morphology set in. It was concluded that a systematic widespread pinch-off of the stretched lamellae occurred as they became unstable due to the increasing interface stretching resistance. Fragmentation was then initiated by thickness irregularity within lamellae. Crystalline fragments then underwent shape change to reduce interface energy, causing rotation of the interface around the centers of the fragments. The transformation eventually led to reconstruction of a new long period along the flow direction.

2. Experimental

2.1 Raw Material Description

The raw UH was obtained from Westlake Plastics (Lenni, P.A.) as a circular, ram-extruded rod with a two-inch diameter. The resin was manufactured by Hoechst Celanese Corporation (Hostalen GUR 4150HP). The molecular weight of 6 million was determined by intrinsic viscosity measurements [10]. The melt flow index was essentially zero.

2.2 Recrystallization of Standards

A recrystallization procedure was performed to establish standard unoriented texture for compression. The raw UH samples were melted at a temperature between 160-170°C for one hour in an oven, then slowly (over approximately 3 hours) cooled down to room temperature inside the oven.

Figure 2-1: Diagram of the Channel Die
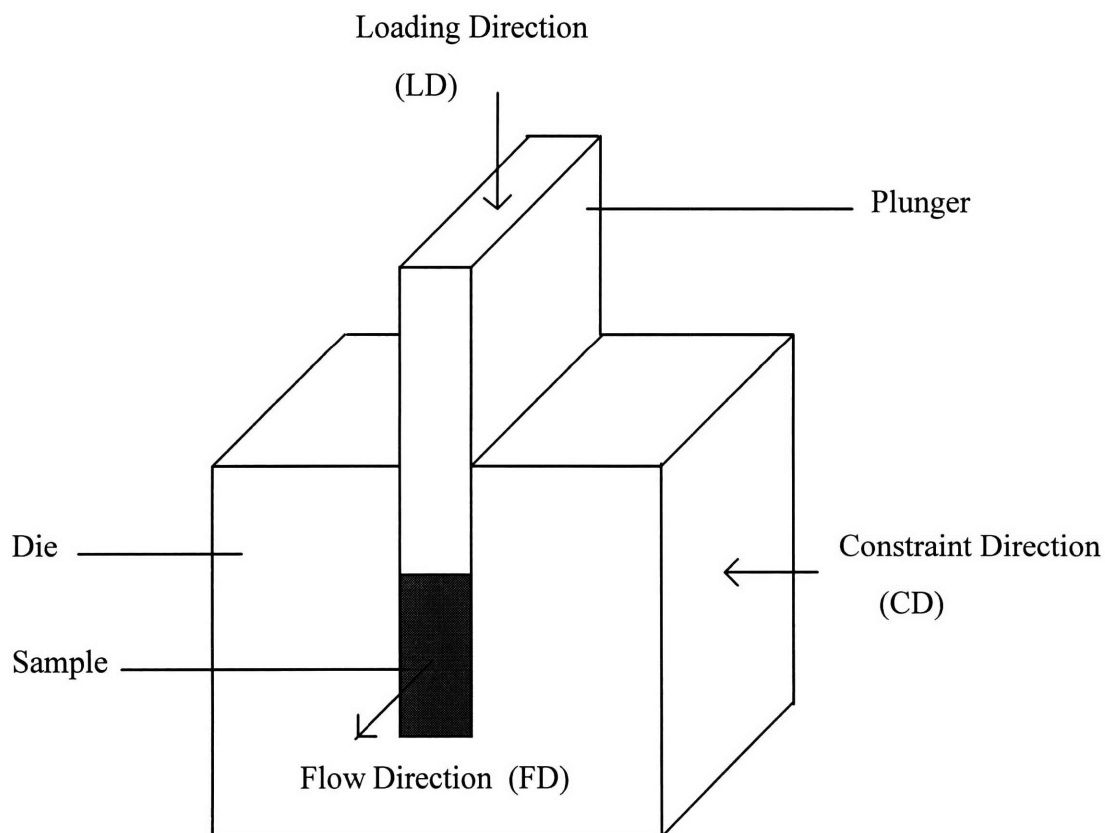
2.3 Channel Die and Compression Condition

Figure 2-1 illustrates the channel die used to perform the plane-strain compression. The deep steel channel die built by Lin and Argon [11] has a channel dimension of 10.5 mm in width and 76.2 mm in length (see reference [11] for more detailed description). Load was applied to a plunger of the same dimension. A pair of heating slabs were used to maintain desired elevated temperature of the system. The die was the same one used for the previous channel die compression study of HDPE by Galeski et al. [1].

Each recrystallized sample was machined to fit snugly inside the channel. All sample-die contact surfaces were lubricated with Dow-Corning high-temperature bearing grease (medium consistency) to minimize friction. During each compression, temperature of the sample was maintained at 80°C. Each sample was compressed at the fixed engineering strain rate of 0.0025 per second until the desired compression ratio - defined by the ratio of original height to the compressed height - was reached. The same compression condition was employed for the compression of HDPE [1] .

Once compressed to a nominal compression ratio, the entire setup was allowed to cool to room temperature while the nominal compression ratio was maintained. The sample was released from the die at room temperature. The instantaneous strain recovery (height expansion) was measured immediately after load release. The sample was then monitored for long-term strain recovery. The series of compressed samples comprise the following nominal compression ratios: 1.4, 1.9, 2.3, 3.2, 4.0, 5.6, and a fractured sample. The compression ratio just prior to fracture was between 6 and 7.

The compressed sample was then machined into three thin slabs, each approximately 1.5 mm thick, corresponding to the three orthogonal directions of the channel die. These samples were used for subsequent X-ray analyses.

2.4 Small-angle X-ray Scattering (SAXS)

2.4.1 SAXS Background

     The scattering of x-rays arises from the non-uniformity of electron density within the sampling medium. In a SAXS experiment, one measures the scattered intensity profile as a function of scattering angle 2θ, using either an area (2D) or a linear (1D) detector. A majority of our data were taken as 2D scattered intensity patterns, except for the 1D profiles obtained from the ultra-SAXS at Brookhaven. These 2D patterns also provide quantitative information on orientation distribution in the plane perpendicular to the incident beam, which is especially useful for investigating anisotropic materials such as our oriented samples.

     Azimuthal integration over the scattering region of interest within a 2D pattern yields a radial average intensity profile, which is plotted as a function of scattering vector $q = (4\pi / \lambda) \sin\theta$, where λ is the X-ray wavelength and θ is half the scattering angle.

     The ultimate purpose for a scattering experiment is to obtain the actual electron density profile within the sample. While this density profile contains all the relevant information about the dimensions - e.g., long period, crystallite thickness, interfacial thickness - of the scattering medium, it is often sufficient to obtain the long period from the scattering curve using Bragg's law.

     The mathematical expression used to transform the experimental scattering profile into the pair distribution function P(x), which is the same as the correlation function in the case of lamellar morphology, is as follows [10]:

$$P(x) \ = \ 1/_{(2\pi^2 A)} \ [\int_0^\infty q^2 \ I(q) \ \cos(qx) \ dq \ ]$$

     It would be ideal if one could successfully derive the pair distribution function from an experimental scattering profile. However, it is not possible, experimentally, to obtain a scattering curve that starts from $q=0$, as one is limited by the ability to resolve the scattered data near the primary beam. Also, is it not possible to obtain data with a tail that extends to $q=\infty$ as one is limited by the detector size and scattered noise. Thus, some method of extrapolation or omission of the two extremes is needed to perform such

transformation. Inevitably, an extrapolation method would incorporate some error into the resulting correlation function.

Therefore, we did not attempt to acquire the actual correlation function. Instead, we resorted to the simple Bragg's scattering law in order to estimate the most probably value of the long period spacing. Such long period was estimated from the peak of the Lorentz-corrected plot - the plot of Iq^2 as a function of q, which takes into account the assumption that lamellae are infinitely large in two directions.

2.4.2 Instruments

Three SAXS instruments were used to perform SAXS measurements. The first two instruments operate with copper $K\alpha$ X-ray of wavelength 1.54 Å.

1. R.E. Cohen Lab (MIT): a Rigaku rotating-anode point source operating at 40kV and 30mA. The beam was collimated with the double-focusing Charles Supper mirrors. The scattered X-rays traveled through a helium-filled cylindrical path (to minimize further scattering from ambient air molecules) to a 2D Siemens detector placed at 130cm from the sample. The detector detected signals within the approximate q-range of 0.06 nm^{-1} up to 0.9 nm^{-1}.

2. Center for Materials Science and Engineering (MIT): a Rigaku rotating-anode operating at 40kV and 100mA (or higher current). The beam was collimated by a cylindrical collimator; scattered X-rays traveled through an evacuated path to a 2D Siemens detector placed at 64.75cm away from the sample. The lower-q resolution was approximately 0.15 nm^{-1}.

3. National Synchrotron Light Source at Brookhaven National Laboratory (Ultra-SAXS, Beam line X23A3): a synchrotron source operating with 10keV X-rays (wavelength = 1.299 Å) and a moving detector. A desmearing procedure was used to obtained the final 1D profile with a ultra-low q-resolution of approximately 0.005 nm^{-1}. (Thus, scattering from large structure such as voids were observed.)

2.4.3 Data Collection and Processing

Table 2-1 shows the details of the conditions under which the different sets of SAXS data sets were taken:

Table 2-1: SAXS Data Sets

Set#	Instrument	Sample(λ)	View Mode	Operating Power
1	R.E. Cohen	1 (standard)	-	40kV * 30mA
2	R.E. Cohen	5.06	CD	40kV * 30mA
		1.95	CD	40kV * 30mA
3	CMSE	5.6	CD, FD, LD	40kV * 150mA
		4.0	CD, FD, LD	
		1.4	CD	
		2.3	CD	
4	CMSE	1.4	FD, LD	40kV * 100mA
		5.06	CD	
		1.95	CD	
5	CMSE	5.06	FD, LD	40kV * 100mA
		1.95	FD, LD	
		2.3	FD	
6	CMSE	3.2	CD, FD, LD	40kV * 100mA
		2.3	LD	
7	Brkhvn	1	-	10 keV
8	Brkhvn	4.0	CD, LD Scans	10 keV
		5.6	CD, LD Scans	

Note that the conditions under which each set of patterns was taken - primary beam intensity, shape, size and alignment; beamstop size and alignment; flight path condition - differed from set to set (e.g., alignments change from day to day for a given machine). Thus, detailed comparisons between patterns could be made mainly between those of the same set.

When the laboratory instruments were used, integrated scattering curves were normalized and subtracted by their respective background curve according to Porod's extrapolation. In the case of ultra-SAXS, absolute intensity calibration obviated such assumptions.

2.5 Pole Figure

2.5.1 Background

Polyethylene forms orthorhombic crystals with the a, b, and c unit cell parameters of 7.4, 4.93, and 2.54 Å respectively. The c-axis is equivalent to the chain axis within the cell. The different crystallographic planes diffract X-ray according to the Bragg's diffraction law: $n\lambda = 2d(\sin\theta)$, where λ, d and θ represent X-ray wavelength, crystallographic plane separation, and Bragg diffraction angle. The Pole figure, a stereographic projection, was employed as the method to map the 3D crystallographic texture with respect to the compression geometry.

2.5.2 Instrument

A Rigaku X-ray diffractometer operating with Cu Kα X-rays of wavelength 1.54 Å was employed. The X-ray point source was generated by a rotating anode at 50 kV and 60 mA; the beam was filtered with a Ni filter. A dedicated MicroVAX computer was used for data collection.

2.5.3 Data Collection and Processing

Pole figures were constructed for the (200), (020) and (002) atomic planes. All measurements covered the α-rotation from $0°$ to $90°$ and the β-rotation from $0°$ to $360°$, both in $5°$ increments. The transmission-to-reflection connection angle for (200) and (020) measurements was $45°$; the connection angle for (002) measurements was $30°$.

To minimize the effects of sample geometry and X-ray absorption, two measurements were done to construct each pole figure. One measurement was done at the diffraction peak for the plane of interest (2θ angle determined by Bragg's law), the other at a 2θ position away from the peak (background). The peak intensity was subtracted by the background intensity, then normalized by the background intensity. The normalized data was scaled from 0 to 10, then plotted into a finished pole figure.

3. Non-X-ray Results

3.1 Stress-Compression Ratio Curves

Figure 3-1 illustrates the curves of stress responses upon channel die-compression of UH and HDPE under the same compression condition: 80°C at a 0.0025-per-second strain rate. The stress was calculated from the ratio of applied load to the area of die channel and the compression ratio was the ratio of original sample height to an instantaneous height during compression. The prominent strain hardening exhibited by UH occurred much more abruptly than HDPE. Compression ratio at fracture of UH, being below 7, was significantly lower than the ultimate compression ratio of HDPE. Yielding in UH also occurred at a lower compression ratio than in HDPE.

3.2 Strain Recovery

Figure 3-2 shows the strain recovery behavior of UH. The linear curve represents the nominal true strains imposed by compression. It was observed that UH exhibited significant relaxation upon being released from the die, resulting in a reduction of strain relative to the imposed strain. Hence, the middle curve represents the true strains immediately after load release. Each compressed UH sample exhibited relaxation over extended time periods; the relaxation became negligible after approximately two months. The lowest curve represents the final true strains of compressed samples.

Note that strain recovery in channel die-compressed HDPE was negligible and, therefore, was not reported in the previous study [1]. The HDPE strain recovery was less than 10% in magnitude of UH's recovery, and only lasted less than 24 hours [12].

Channel-die Compression
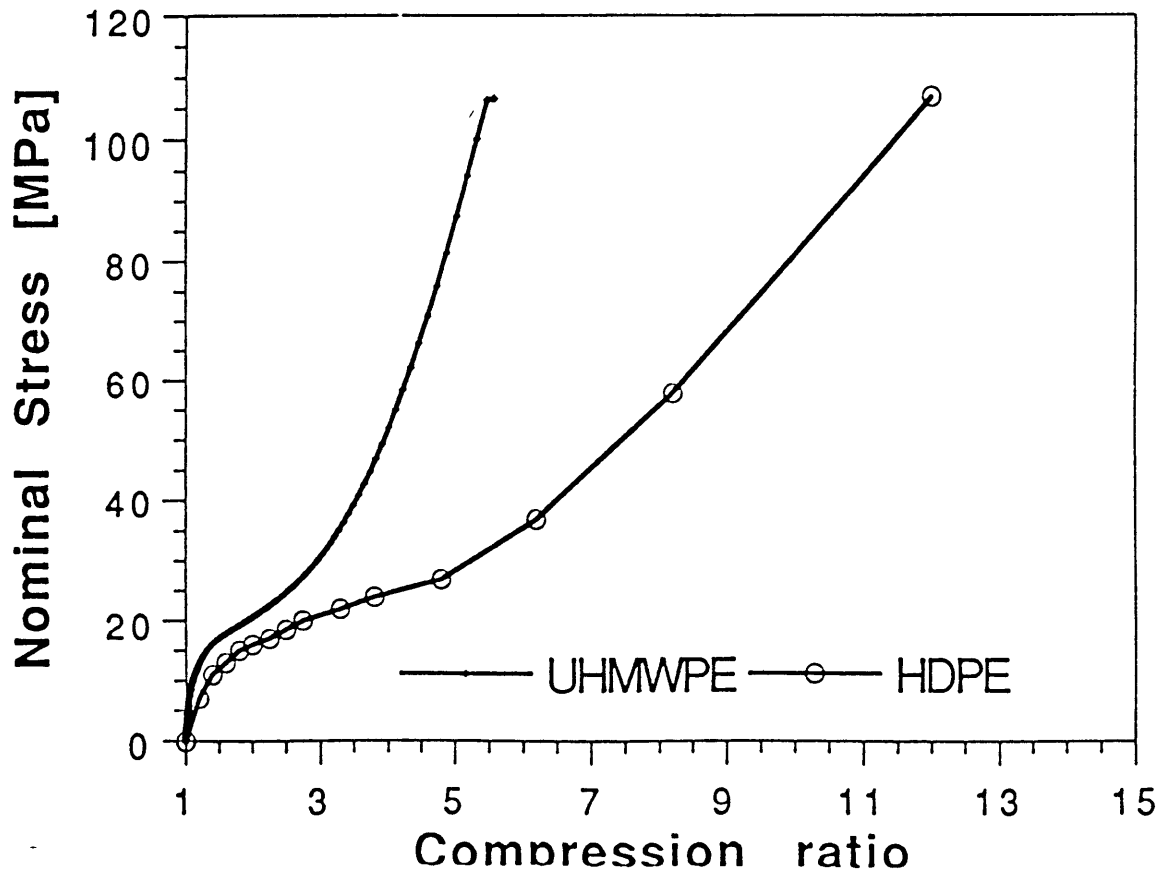
Figure 3-1: Stress-Compression Ratio Curves of
Channel Die-Compressed UH and HDPE
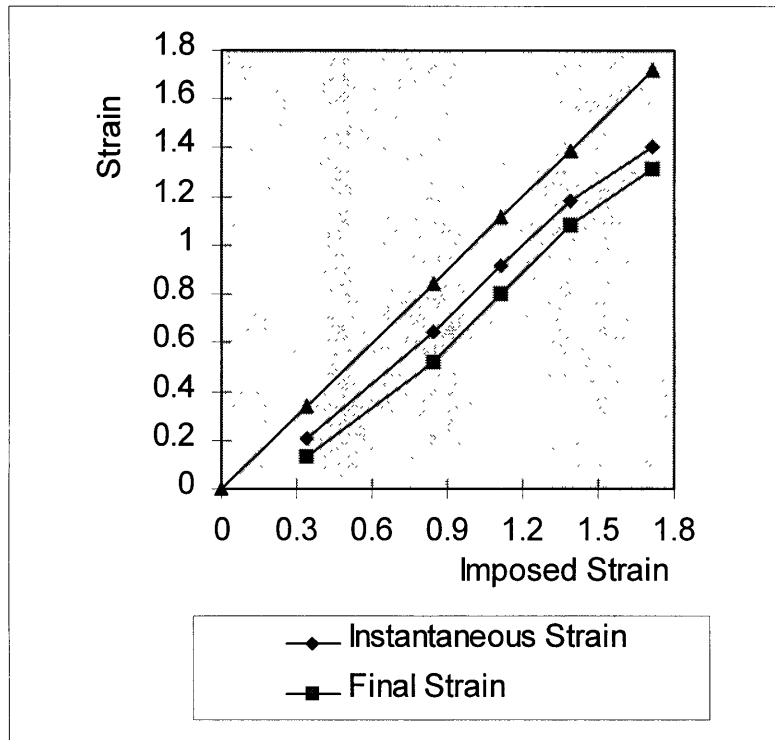
Figure 3-2: *Strain Recovery of Channel Die-Compressed UH: Instantaneous and Final Strains*

3.3 Differential Scanning Calorimetry

Table 3-2 shows the degrees of crystallinity of the standard and the compressed samples. The degree of crystallinity was determined based on the heat of fusion of 293 J/g of linear polyethylene crystal [13]. The data showed slight increase in the degree of crystallinity at low compression ratios. The degree of crystallinity decreased towards higher compression ratios. The fractured sample shows approximately 7% drop in crystallinity relative to the standard. Note that the degree of crystallinity of the standard sample was determined after the sample had been stored in the channel die at 80°C without being compressed to ensure the same thermal cycles as the compressed samples.

Table 3-2: *Degree of Crystallinity Determined using DSC*

Sample	ΔH_{fus} (J/g)	Crystallinity(%)
Standard ($\lambda = 1$)	142.9	48.8
$\lambda = 1.4$	143.14	48.9
$\lambda = 1.95$	144.15	49.2
$\lambda = 3.2$	131.66	44.9
$\lambda = 4.0$	129.56	44.2
$\lambda = 5.6$	124.93	42.6
Fractured	123.23	42.1

4. SAXS Results

Figure 4-1 illustrates the SAXS scattering pattern of the standard. Figures 4-2 to 4-5 illustrate the patterns of the compressed samples viewed along the three orthogonal directions. Summaries of their important features are as follows:

$\lambda=1$ Figure 4-1 illustrates the isotropic (ring) pattern which implies a randomly distributed lamellar structure. The Lorentz-corrected curves of the standard sample (Figure 4-6) obtained from data sets #1 and #7 (see Table 2-1) yielded a consistent estimate for a period spacing of 500 Å.

$\lambda=1.4$ Without significant alteration from the isotropic pattern, the CD-view pattern (Figure 4-2a) shows a slight elongation of scattered intensity along LD. Integration of the pattern showed higher scattered intensity along LD than along FD. This indicated simultaneous thinning and rotation of long period towards LD in response to plane strain compression, though the majority of lamellae were randomly distributed.

$\lambda=1.95$ The CD-view pattern in Figure 4-2b shows increased elongation of the two-point pattern along LD and a reduction of intensity along FD. This indicates that an increasing number of lamellar normals had clustered towards LD with a simultaneous reduction in long period. In addition, a trace of a four-point pattern was observed.

$\lambda=2.3$ Figure 4-2c illustrates development of the four-point pattern as it becomes more prominent in the CD-view pattern.

$\lambda=3.2$ From Figure 4-2d, the four-point pattern appeared prominent, suggesting the formation of kinked 'chevron' lamellae, while the scattered intensity along FD had noticeably reduced relative to that of the standard. Continued thinning of LD long

periods was confirmed by further elongation along LD of the FD-view pattern (Figure 4-4c).

$\lambda=4.0$ The CD-view pattern (Figure 4-3a) depicts two prominent lamellar populations: lamellae whose normals align with LD, and those whose normals are, on average, oriented at an angle of 28° to LD. Averaged long period spacing along LD obtained from the Lorentz-corrected plot of data set #8 (Figure 4-7) was 370 Å. This was significantly larger than the 150 Å estimated long period of the 'chevron' lamellae obtained from the Lorentz-corrected plot of the integrated intensity of the four-point streaks (Figure 4-8). This was expected since the LD streaks appeared much nearer to the primary beam than the four-point streaks.

$\lambda=5.6$ From the CD-view pattern (Figure 4-3b), further development of the four-point streaks was evident as they became the most prominent feature of the pattern. Lorentz-corrected plot of these four-point streaks (Figure 4-8) yielded a reduced estimate of the 'chevron' long period at 135 Å. The scattered intensity along FD was very low, essentially indicating the absence of lamellae whose normals align with FD at this high compression ratio.

        The CD-view pattern illustrates the drop in intensity of the LD streaks relative to λ of 4.0, indicating a decrease in the population of lamellae with normals along LD. The ultra-SAXS scan along LD (Figure 4-9) shows the drop in absolute intensity of the LD streaks towards λ of 5.6 (streaks located approximately at $q = 0.17$ nm^{-1}.) Notice the evidence of void-scattering at very low q-range. In addition, emergence of diffused patterns of intensity along LD but further away from the center was observed in both the CD-view and FD-view (Figure 4-4e) patterns; hence, double lamellar populations along LD. This was confirmed by the Lorentz plot (Figure 4-7) of the LD-scan intensity profile (data set #8) which exhibited two maxima: one corresponding to a 390 Å long period, and the corresponding to a 145 Å long period.

The fractured sample, having compression ratio between 6 and 7, showed negligible further development of the morphology from λ of 5.6 (Figure 4-3c). Overall, the monotonic decrease of scattered intensity of the LD-view patterns with increasing compression ratio indicated continuing elimination of lamellae aligned parallel to LD, particularly those with long periods along CD (Figures 4-5).
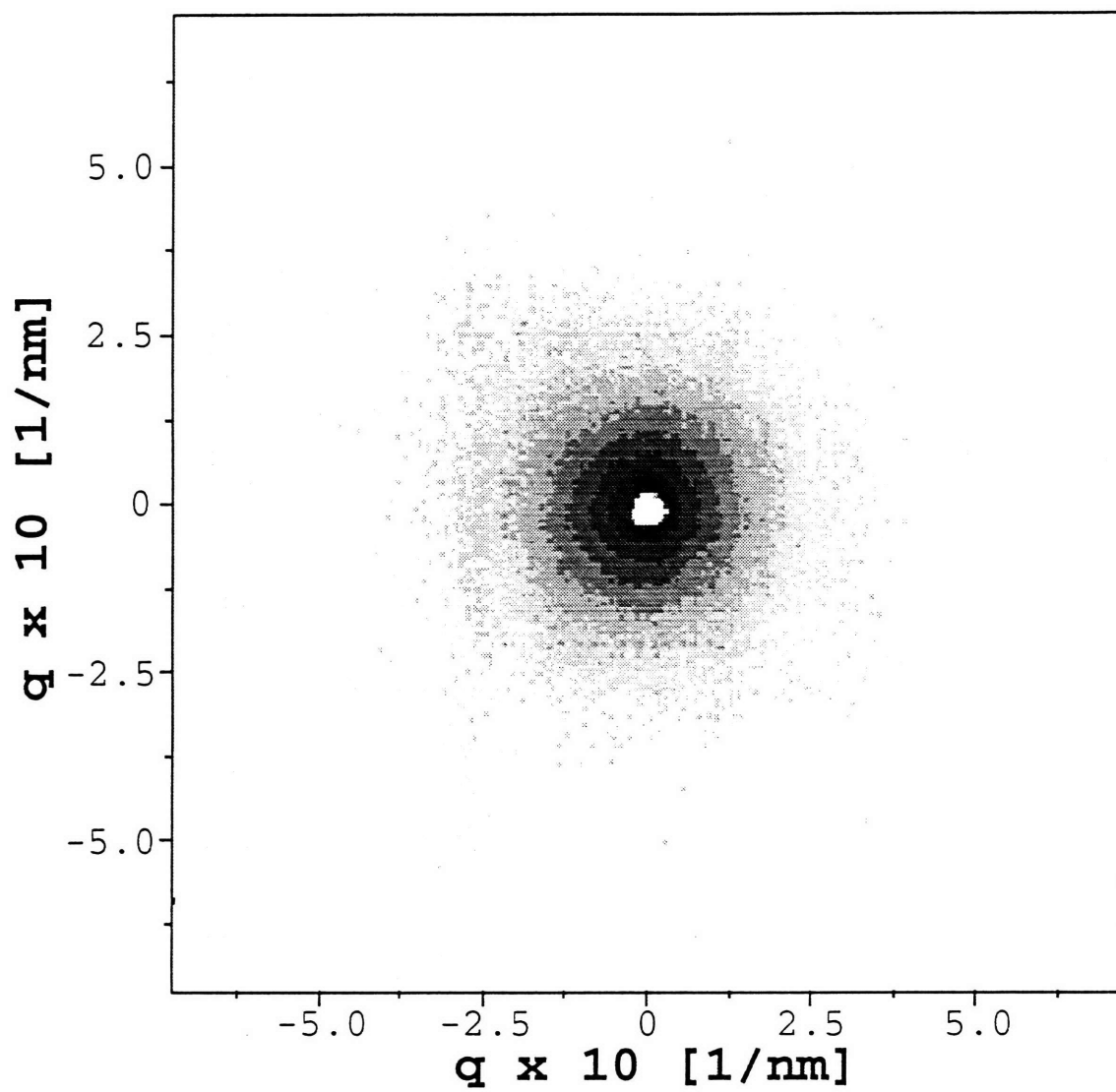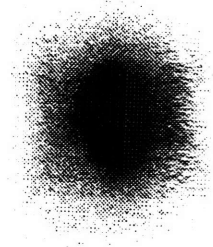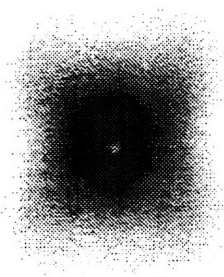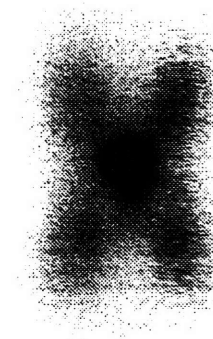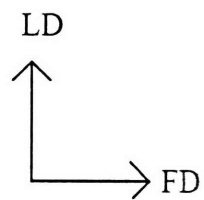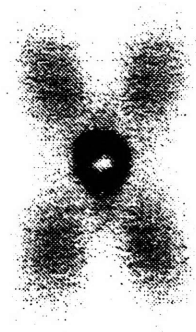
Figure 4-1: SAXS Pattern of Unoriented Standard Sample

a.

b.

c.

d.

LD
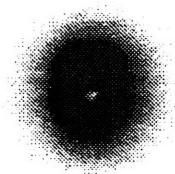
FD

Figure 4-2: *CD-View SAXS Patterns of Compressed UH Samples*
(a) λ=1.4, (b) λ=1.95, (c) λ=2.3, (d) λ=3.2

LD

FD
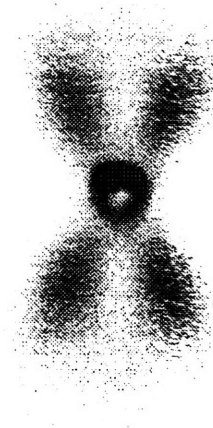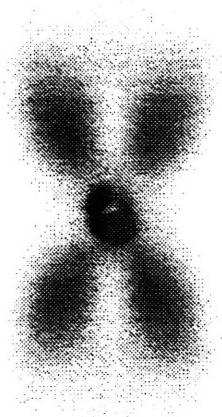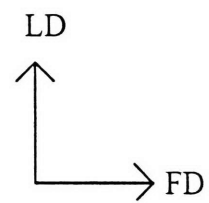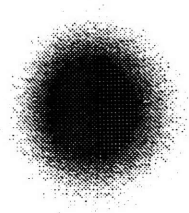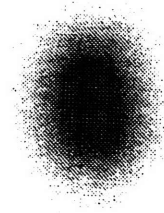
Figure 4-3: CD-View SAXS Patterns of Compressed UH Samples
(a) λ=4.0, (b) λ=5.6, (c) Fractured Sample
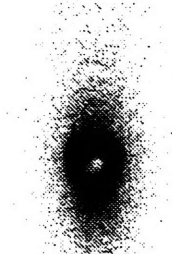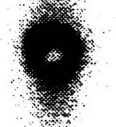
Figure 4-4: FD-View SAXS Patterns of Compressed UH Samples
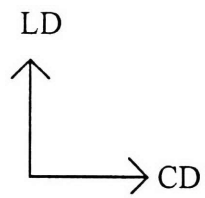*(a) λ=1.4, (b) λ=2.3, (c) λ=3.2, (d) λ=4.0, (e) λ=5.6*

CD
↑
→ FD
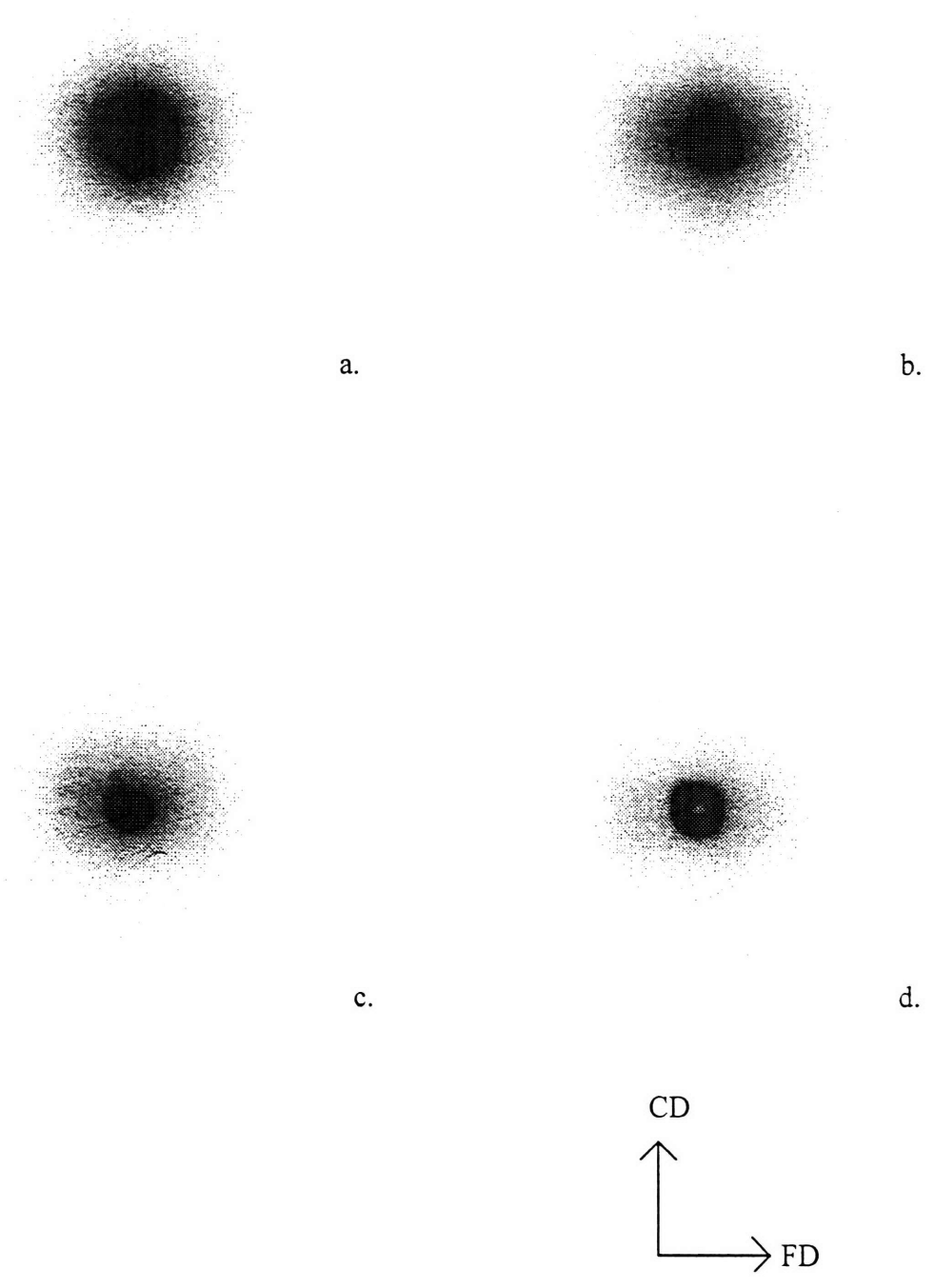
Figure 4-5: LD-View SAXS Patterns of Compressed UH Samples
(a) λ=1.4, (b) λ=1.95, (c) λ=3.2, (d) λ=5.6
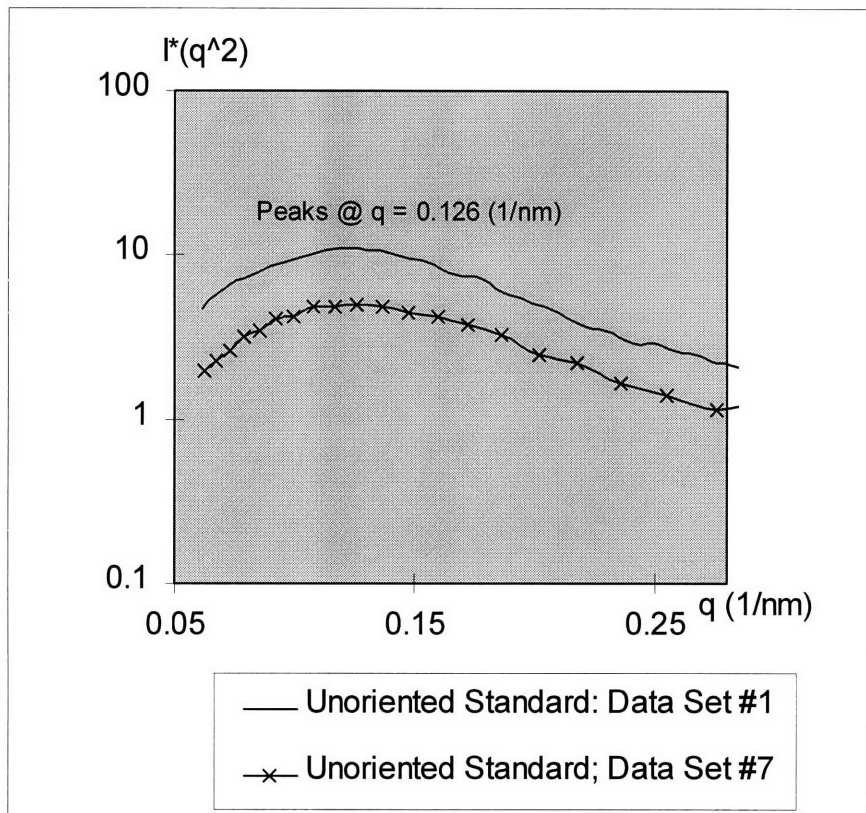
Figure 4-6: *Lorentz-Corrected Curves of Unoriented Standard Sample*
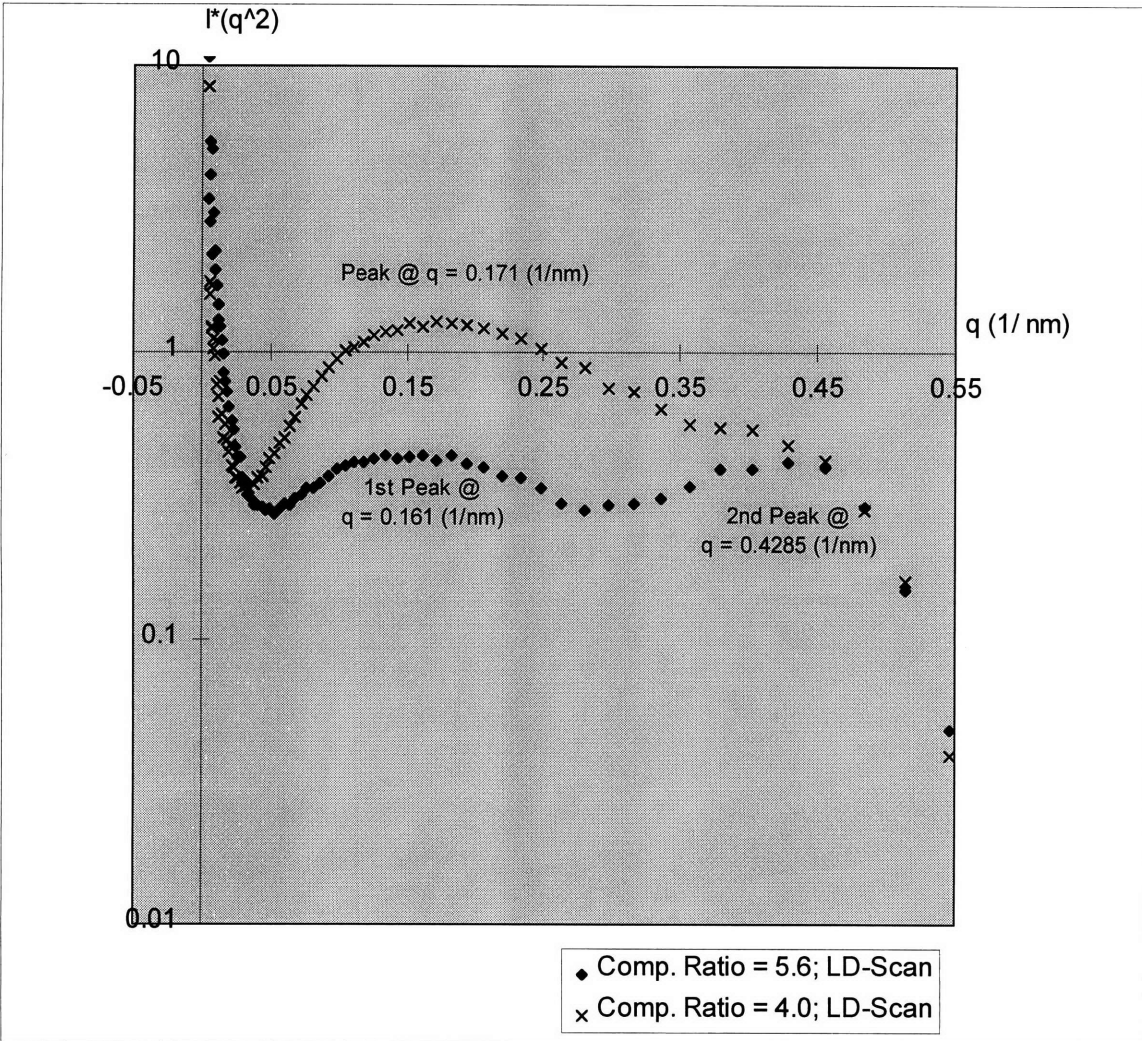
Figure 4-7: *Lorentz-corrected Curves; Ultra-SAXS LD-Scans;* $\lambda=4.0$ *and* $\lambda=5.6$
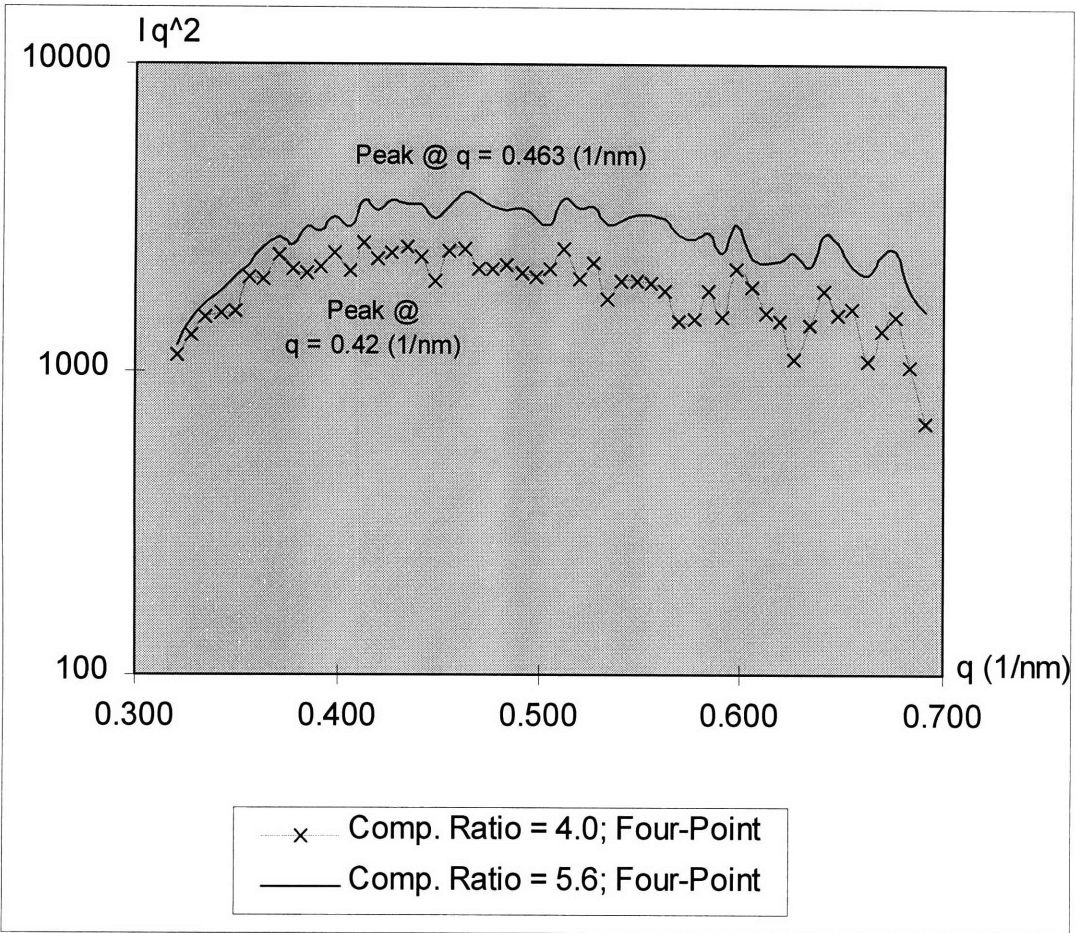
Figure 4-8: *Lorentz-corrected Curves; Integrated Intensity of the Four-point Streaks; λ=4.0 and λ=5.6*

Figure 4-9: *Absolute Intensity Curves; Ultra-SAXS; Unoriented Standard, λ=4.0, λ=5.6*

5. Pole Figure Results

Figures 5-1 to 5-6 illustrate the pole figures of the UH samples compressed to λ of 1.4, 1.95, 2.3, 3.2, 4.0, and 5.6, respectively. Following is the interpretation of the results:

λ=1.4   Despite the low nominal compression ratio, a significant degree of crystallographic orientation had been achieved. The c-pfg showed that c-axes (the chain axes) had clustered towards FD along LD-FD plane, whil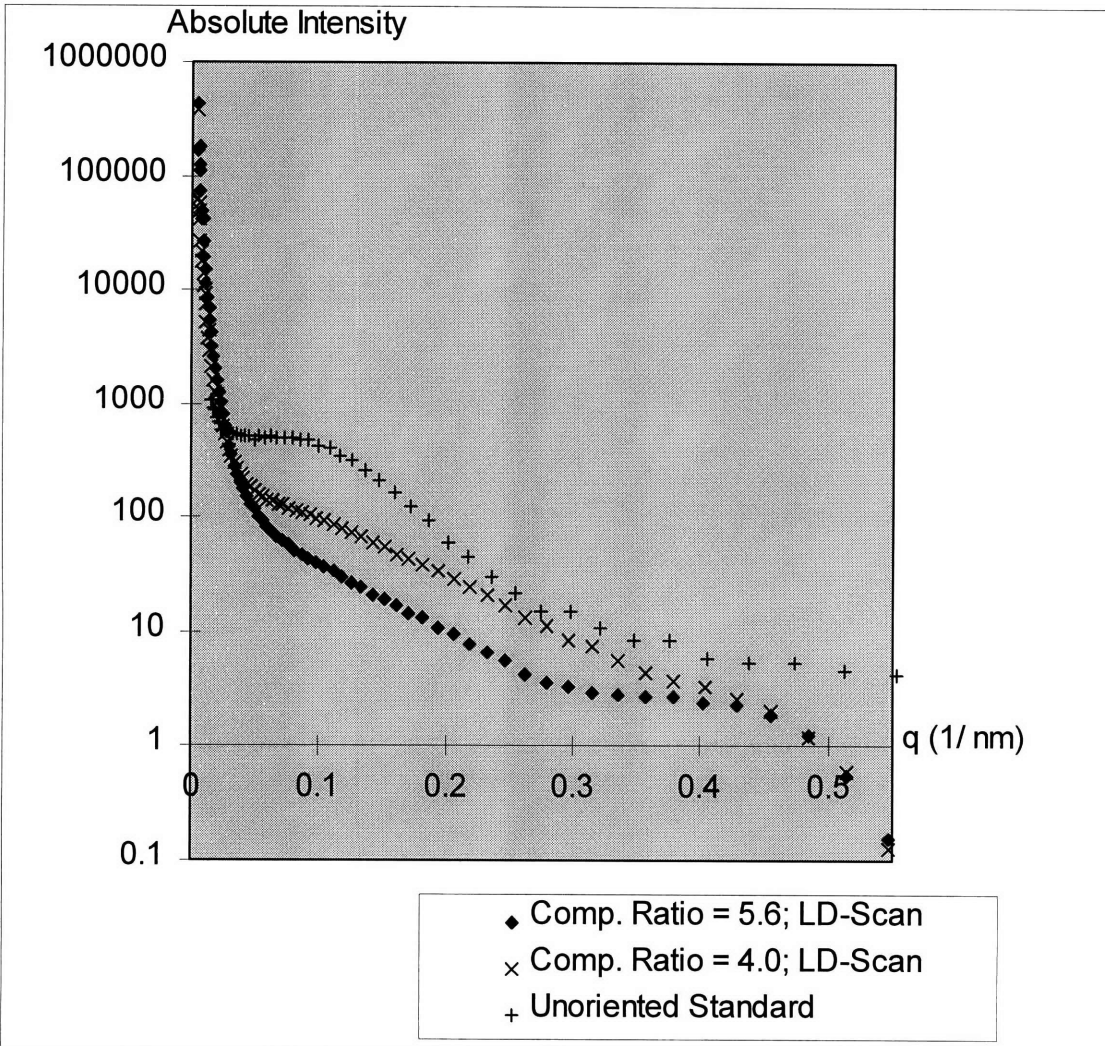e the a-pfg showed that the maxima were along LD, both suggesting the activity of the dominant (100)[001] chain slip. The b-axes clustered towards CD, indicating that the cooperative (100)[010] transverse slip had been already activated. UH texture at this λ correlates best to that of channel die-compressed HDPE with λ of 1.55 [1].

λ=1.95   The cooperative (100)[001] and (100)[010] slips account for the clustering of c-axes further towards FD from LD, and b-axes rotation away from FD. Notice maximum clustering of b-axes had already shifted towards CD. The UH crystallographic texture at this λ correlates best to HDPE texture compressed to λ of 2.5 [1]. The a-pfg showed that the location of maximum clustering had shifted by 20° towards FD, resulting in worse orientation of the a-axes along LD than at λ of 1.4. This implies 'locking' of interlamellar amorphous sliding, which is the coupling counterpart of (100)[001] chain slip. A similar effect of locking of amorphous shear was observed in HDPE at λ of 1.55 [1].

λ=2.3   The texture correlates best to the HDPE texture at λ of 3.13 [1]. It featured more intensive clustering of c-axes towards FD from LD, suggesting further activity of the (100)[001] dominant slip; the activity of the (100)[010] slip accounts for b-pfg evolution. The a-axes clustered further towards LD as the location of absolute

maxima moved by $10°$ back to LD - an expected result of the (100)[001] slip. In addition, notice the spreading of the a-axes towards CD from the LD-FD plane.

$\lambda=3.2$ The a-axes rotated further away from FD, indicating continually increasing (100)[001] slip activity. Though the absolute maxima were located at $90°$ away from FD at this point, they had also moved away from LD to a position nearly half way between LD and CD. Development of a fibrillar-like texture was observed in HDPE at a much higher λ of 12, but to a much lesser extent.

$\lambda=4.0 \& 5.6$ Continuing on up to higher compression ratios, the fibrillar-like texture observed in a-pfg developed into the most prominent feature of the a-pfg: the absolute maxima eventually located themselves at $45°$ between LD and CD. This suggested that another crystallographic deformation mechanism not observed in channel die-compressed HDPE, possibly twinning or martensitic transformation, was responsible for the evolution of the a-axes texture. The activities of the intense (100)[001] slip and the cooperative (100)[010] slip were responsible for the texture evolution otherwise: the a-, b-, and c-axes further clustered towards LD, CD, and FD, respectively.
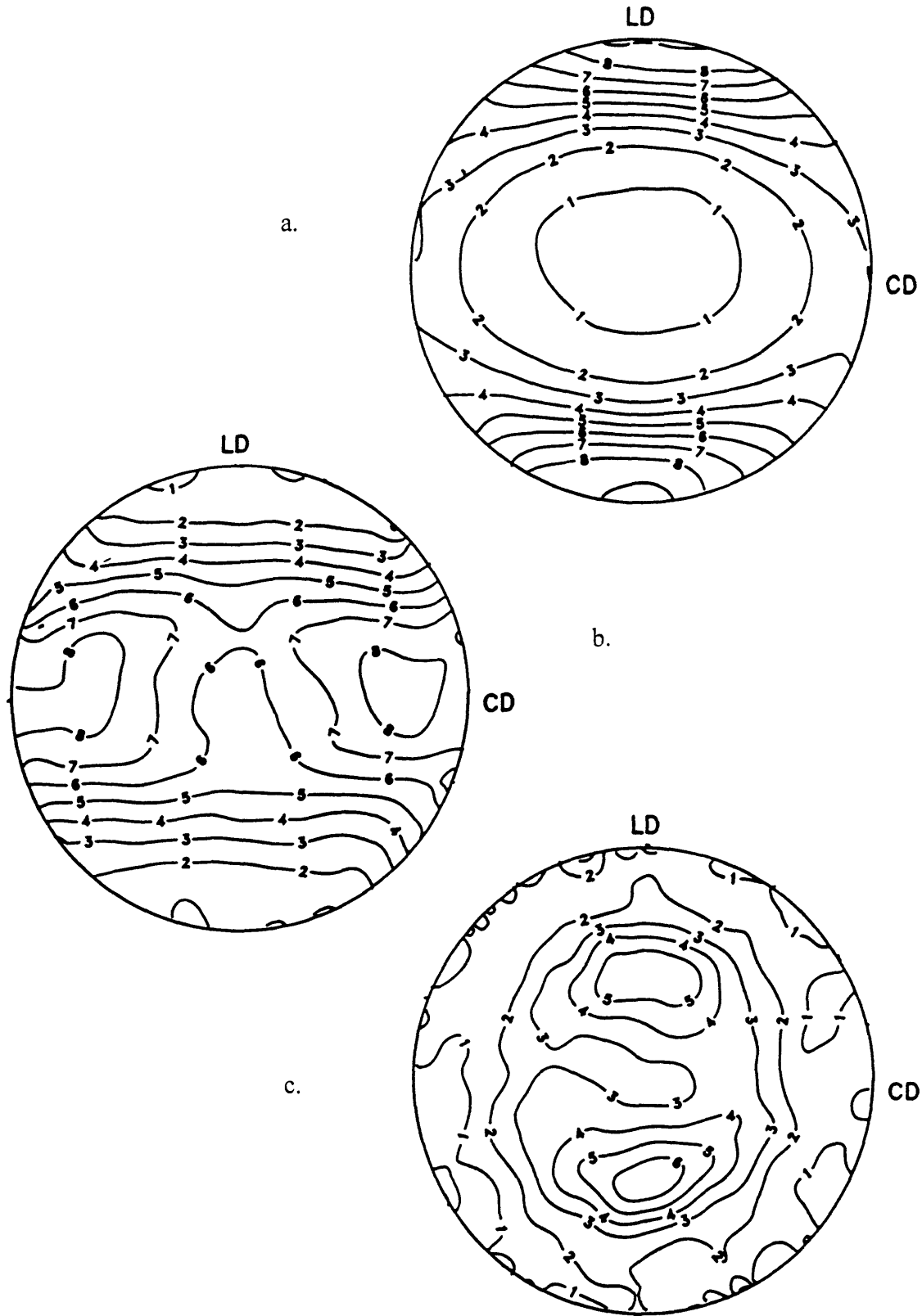
Figure 5-1: *Pole Figures*; $\lambda = 1.4$; *(a) a-axes, (b) b-axes, (c) c-axes*
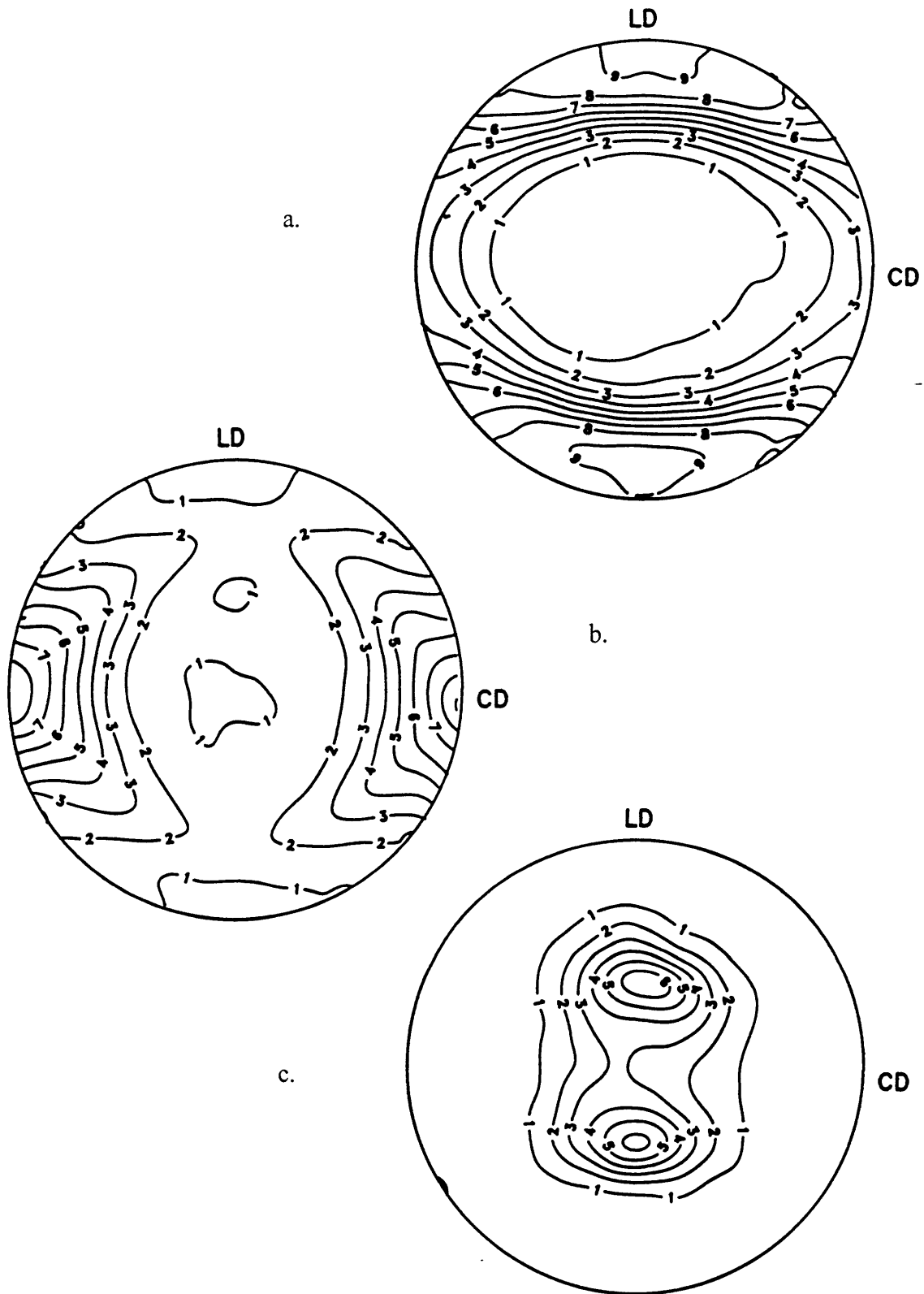
Figure 5-2: Pole Figures; λ = 1.95; (a) a-axes, (b) b-axes, (c) c-axes
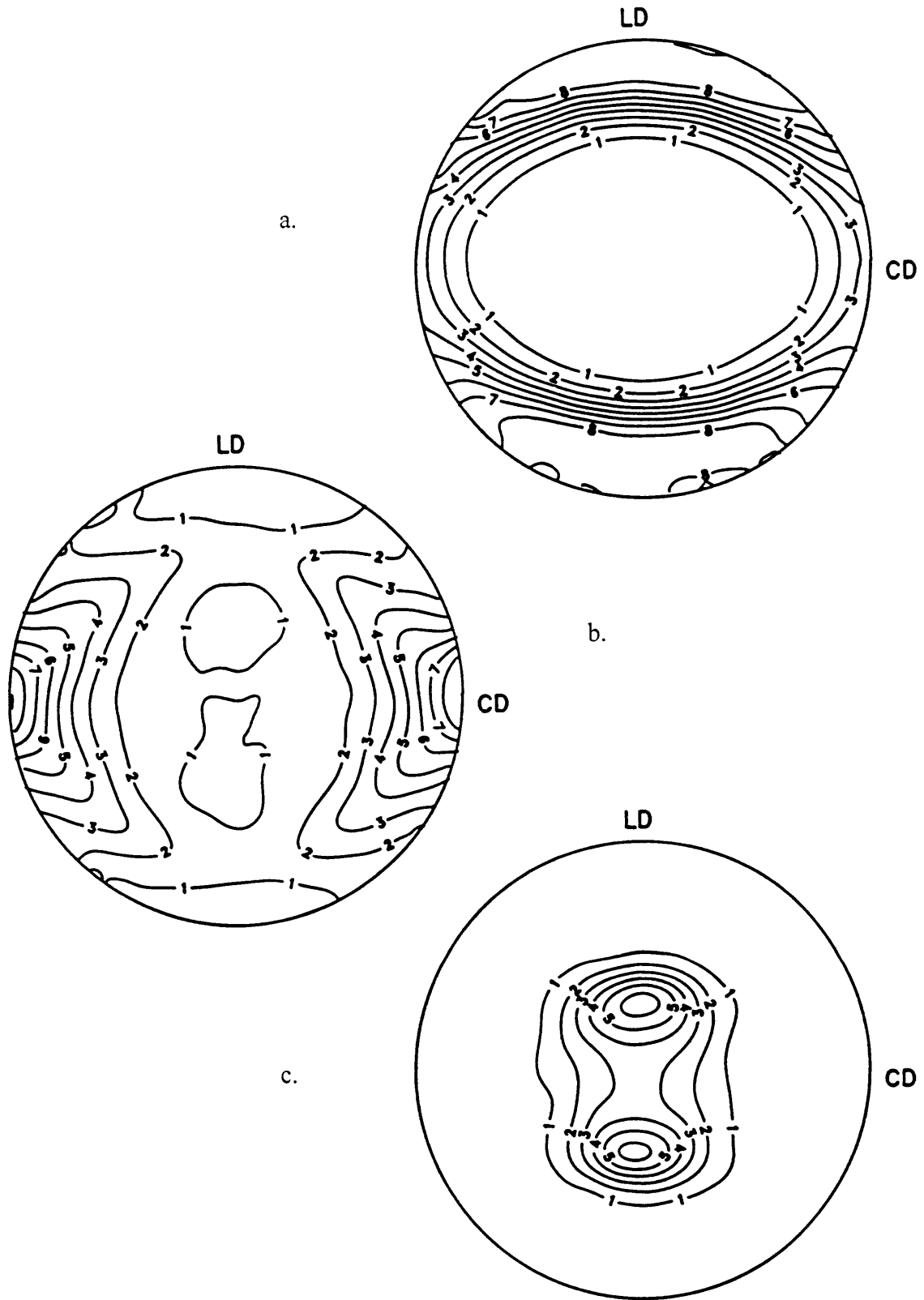
Figure 5-3: Pole Figures; λ = 2.3; (a) a-axes, (b) b-axes, (c) c-axes
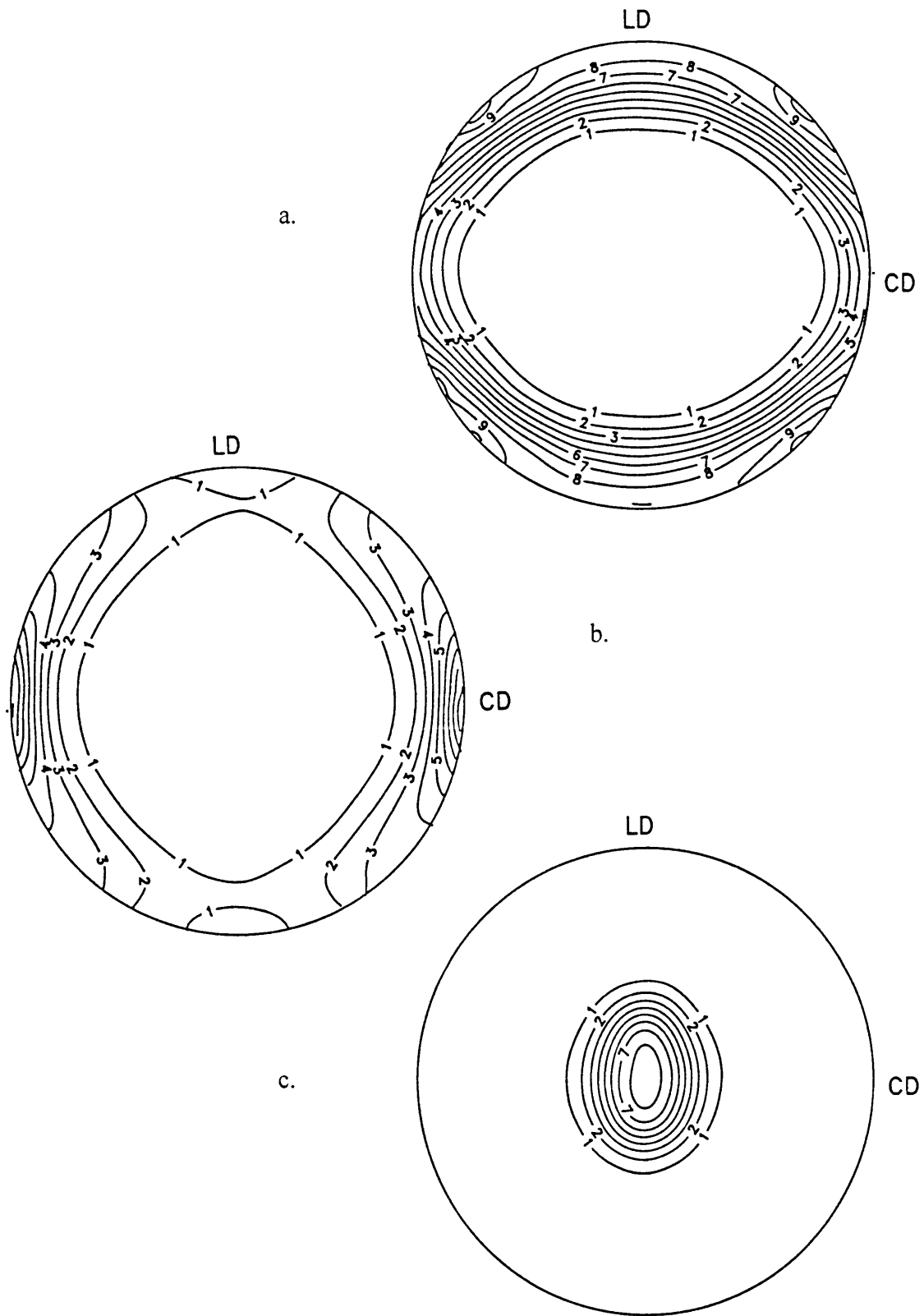
Figure 5-4: *Pole Figures;* $\lambda = 3.2;$ *(a) a-axes, (b) b-axes, (c) c-axes*

Figure 5-5: *Pole Figures;* λ = *4.0;* *(a) a-axes, (b) b-axes. (c) c-axes*

39

Figure 5-6: *Pole Figures;* λ = 5.6; *(a) a-axes, (b) b-axes, (c) c-axes*

6. Discussion

6.1 Comparison with HDPE

6.1.1 Stress Response and Strain Recovery
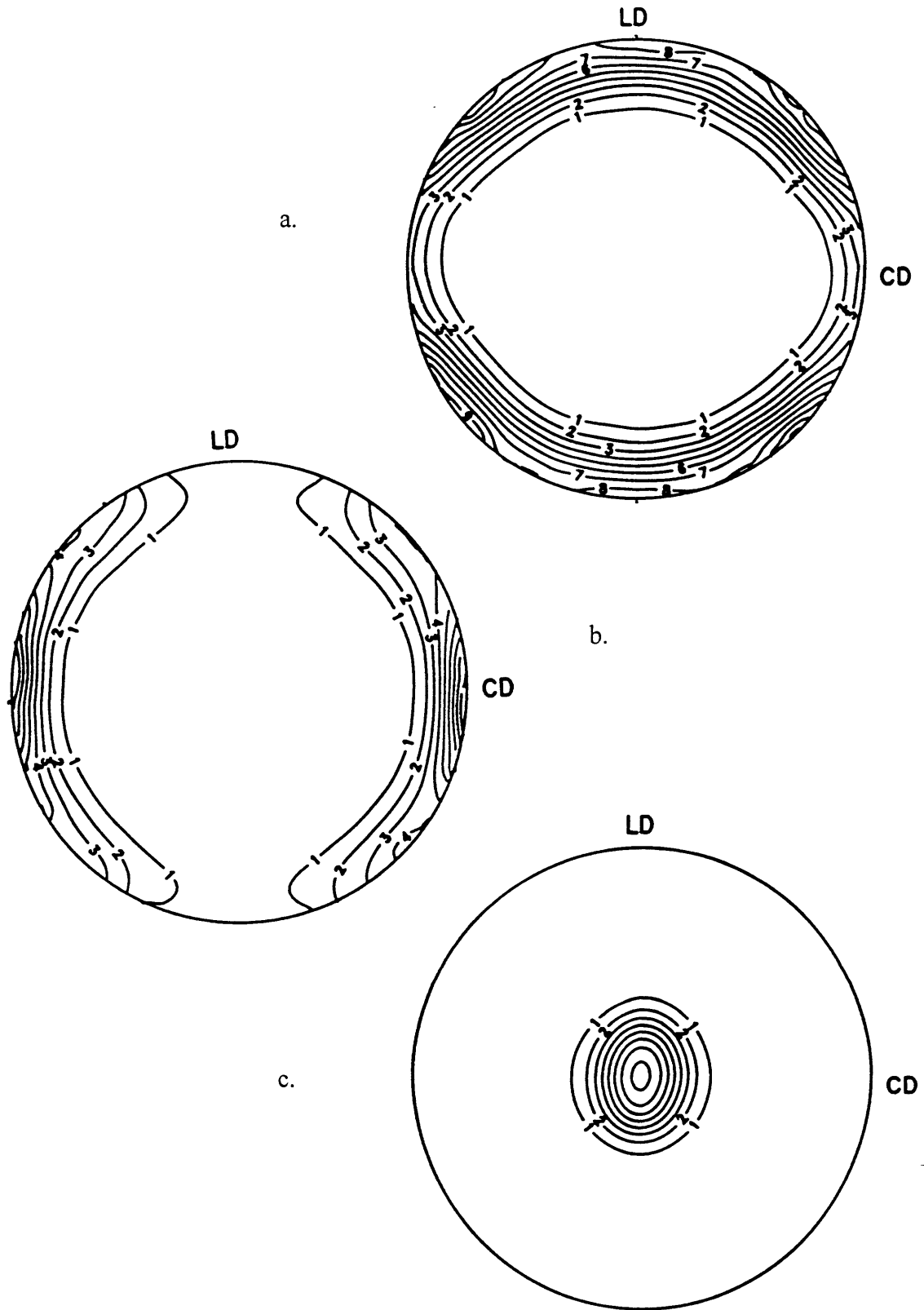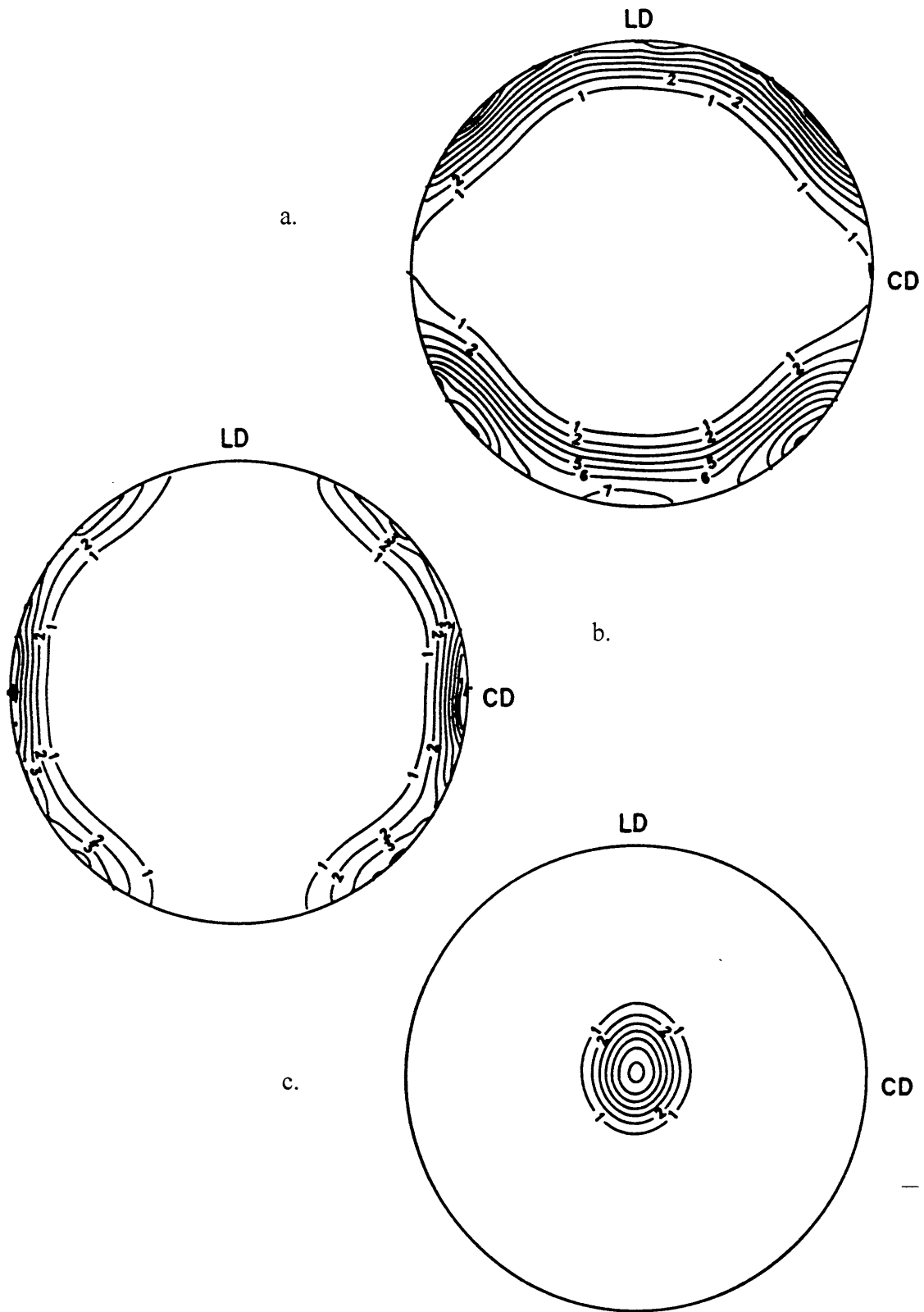
Compared with HDPE compressed under the same compression condition, strain-hardening in UH occurred much more abruptly, and fracture also occurred at a much lower ultimate compression ratio. Yielding took place at lower compression ratio in UH than in HDPE. UH strain recovery occurred to a significantly larger extent and over a long time period, while HDPE did not exhibit significant strain recovery after compression. These unique features indicate higher resistance to deformation of UH relative to HDPE.

6.1.2 Crystallographic Texture

Comparison of UH and HDPE pole figures shows that up to λ of about 2.3, the crystallographic texture evolution in plane strain-compressed UH can roughly be correlated with those of plane strain-compressed HDPE. Therefore, similar to HDPE, the contribution to orientation was primarily from the (100)[001] chain slip, and secondarily from the (100)[010] transverse slip. Evidence of locking of the interlamellar sliding was present between λ of 1.4 and 1.95.

However, each of the three compressed samples of UH correlated with a compressed HDPE sample of a higher compression ratio. This implies earlier crystallographic texturing of UH with respect to that of HDPE, despite more severe relaxation exhibited by compressed UH, which could have caused some loss of orientation upon load release.

Significant deviation of UH crystallographic evolution from the HDPE evolution arose by λ of 2.3, where the maxima in the a-pfg moved away from LD towards CD. Eventually, the maxima was at a 45° angle between LD and CD, while secondary maxima occurred along LD. This indicates that an additional deformation mechanism working simultaneously with the two cooperative slips was responsible for the fibrillar-like texture

of compressed UH, which did not occur in HDPE. In comparison, the HDPE texture developed nearly monotonically towards that of a monocrystal up until the highest λ of 12, where a trace of fibrillar texture was observed in b-pfg figure. Notice that HDPE fibrillar texture formed at much higher λ than in the UH case.

6.1.3 Morphological Texture

The elongation of CD-view SAXS pattern along LD in UH did not occur as extensively as in HDPE. A four-point pattern formed and superimposed onto the two-point pattern along LD at lower λ, indicating two prominent lamellar populations. This implies that only those lamellae whose normals were originally nearly parallel to LD rotate their normals - and thin down simultaneously - towards LD. Early formation of the UH four-point pattern at λ of 1.95 for UH, compared to λ of 3.13 for HDPE, implies relatively early kinking of the UH lamellae.

Subsequent development of the UH chevron morphology, which gave rise to the four-point SAXS pattern, occurred at the expense of lamellae whose normals initially aligned near FD, evident from decreasing scattered intensity along FD. In addition, the long period obtained from the two-point pattern along LD was significantly larger than that from the four-point pattern, indicating that kinked lamellae underwent more extensive slip shear than those LD lamellae. Both features support the proposed formation of the chevron morphology via lamellar kinking and shearing.

Note that the development of the well-defined four-point pattern in UH - i.e., they were azimuthally narrow and the azimuthal angle between two adjacent arms are consistent, though significantly spread-out in radial direction - indicated that the kinked lamellae which gave rise to the pattern were quite large and that their normals formed an angle of about 28° to LD. In contrast, the four-point pattern exhibited by HDPE was relatively diffused. As concluded by Galeski et al. [1], the HDPE four-point pattern arose from fragmented lamellar blocks undergoing morphological transformation leading to a new long period along FD. The fact that our compressed UH samples exhibited the well-defined four-point pattern up to the highest attainable degree of deformation (i.e., SAXS

pattern of a fractured sample) indicates absence of such restructuring transformation in UH.

6.2 Global Viewpoint

The difference in the structure of HDPE and UH, which results from the difference in molecular weight, gives rise to their different deformation behaviors. As mentioned earlier, we contribute this mainly to the difference in the two amorphous regions, particularly the amount of tie molecules.

Tie molecules are molecules that are incorporated into multiple crystals, or ones that form loops with molecules of other crystals [14]. The amount of tie molecules can be controlled by crystallization process. Essentially, crystallization process that allows for adjacent reentry of a chain back into the same crystal results in crystals with relatively few tie chains (e.g., solution crystallization). On the other hands, such process in which the ability for molecules to chain-fold is hindered results in greater number of tie chains.

As an indirect evidence of effects of number of tie molecules and degree of chain folding, it has been observed that quench-crystallized polyethylene resulted in enhanced toughness and strain hardening [14]. In this case, the ability for each chain to reptate through the melt and to incorporate itself in a single, chain-folded crystals is suppressed by the increased rate of crystallization. This contributed to an increased number of tie molecules connecting multiple lamellae, leading to increased toughness.

In our comparative HDPE and UH systems, molecular weight is the variable contributing to the difference in the two crystallization processes. Upon crystallization from the melt, the ability for larger molecules - such as ones of UH - to reptate is more hindered than smaller ones. Thus, one can imagine that UH chains are more likely to be incorporated into multiple crystals than HDPE chains; hence, larger number of tie molecules. This is evident from higher toughness and lower degree of crystallinity of UH relative to HDPE.

In rationalizing the deformation of UH, it is useful to draw an analogy of our comparative systems to the well-established knowledge of deformation of elastomers since we feel that the unique deformation behavior of UH is attributed to the properties of

43

its amorphous region. The PE glass transition, which is well below room temperature, renders elastomeric nature to the amorphous region. A simple analogy can be drawn between UH amorphous region and a crosslinked rubber, and between HDPE amorphous region and a lightly crosslinked rubber, since there are larger number of tie molecules and more entanglements in UH amorphous region.

Higher resistance to plastic deformation in the UH amorphous region is attributed to higher entanglement density and smaller number of loose chain ends. A larger number of tie molecules contribute to higher degree of connectivity between adjacent lamellae. Note that it is legitimate to correlate entanglements to physical crosslinks since the timescale of deformation employed was not infinite. Thus, disentanglement need not be accounted for.

High entanglement density and high degree of connectivity are responsible for early activation of crystallographic slip mechanisms in UH. Early development of the lamellar kinking to form the chevron morphology can be accounted for in the same way: smaller number of UH lamellae were able to rotate their normals towards LD before their rotation became restricted and kinking became necessary to accommodate further strain.

Larger strain recovery results because the oriented UH molecules are less capable of undergoing disentanglement upon deformation. Therefore, a larger amount of recoverable strain energy is stored by entanglements which act as physical crosslinks. High entanglement density accounts for more abrupt strain hardening, in analogy to the effect of increasing crosslink density on strain hardening of elastomers. Higher entanglement density is also responsible for the absence of restructuring transformation: it causes strain hardening that leads to macroscopic fracture of the material prior to initiation of lamellar 'pinch-off' due to stretching instability, which was observed in HDPE.

Unique development of fibrillar-like texture in the a-pfg, and development of well-defined chevron morphology, were most likely initiated due to properties of the UH amorphous region. The underlying mechanisms of these developments, which were not detected in HDPE, need further investigation to be identified.

7. Conclusion

We were able to induce a large degree of chain alignment along the flow direction in UH using channel die compression, despite the fibrillar-like texture observed in the a-pfg. This rendered channel die compression a suitable method for producing oriented samples for future wear tests.

The previous study by Galeski et al. [1] provided a basis for comparison to the deformation behavior of UH. We determined that most of the mechanisms underlying the crystallographic evolution of HDPE were also responsible for the crystallographic texturing in UH. The onset of crystallographic and morphological texturing occurred earlier - that is, at lower compression ratios - in UH than in HDPE. In addition, greater resistance to deformation and more extensive strain recovery were exhibited by UH. Unlike HDPE, UH lamellar morphology did not undergo restructuring transformation even up until the point of fracture. Instead, SAXS pattern indicated formation of well-defined chevron morphology.

The analogies drawn between the amorphous region of the two materials and crosslinked elastomers were useful in rationalization of the unique deformation behavior of UH. In summary, larger number of tie molecules and higher degree of entanglement within UH amorphous region - a direct effect of its high molecular weight - accounted for higher resistance to deformation and early texture evolution of UH relative to HDPE.

8. References

1. Galeski, A.; Bartczak, Z; Argon, A.S.; Cohen, R.E. *Macromolecules* **1992**, 25, 5705.

2. Anderson, J.C. *Tribology International* **1982**, Feb., 43.

3. Bowden, P.B.; Young, R.J. *J. Mater. Sci.* **1974**, 9, 2034.

4. Peterlin, A. *J. Mater. Sci.* **1971**, 6, 490.

5. Keller, A.; Pope, D.P. *J. Mater. Sci.* **1971**, 6, 453.

6. Young, R.J.; Bowden, P.B. *Phil. Mag.* **1974**, 29, 1061.

7. Argon, A.S.; Bartczak, Z.; Cohen, R.E.; Galeski, A.; Lee, B.J.; Parks, D.M. "Deformation induced texture development in polyethylene: computer simulation and experiments." Oriented Polymer Materials. Ed. Fakirov, S. Huthig & Wepf: New York, 1996, pp. 265-301.

8. Bartczak, Z.; Cohen, R.E.; Argon, A.S. *Macromolecules* **1992**, 25, 4692.

9. Bartczak, Z.; Argon, A.S.; Cohen, R.E. *Macromolecules* **1992**, 25, 5036.

10. Bellare, A.; Schnablegger, H.; Cohen, R.E. *Macromolecules* **1995**, 28, 7585.

11. Lin, L.; Argon, A.S. *Macromolecules* **1992**, 25, 4011.

12. Bartczak, Z., private communication.

13. Wunderlich, B.; Cormier, C.M. *J. Polym. Sci., Polym. Phys. Ed.* **1967**, 987.

14. Knight, G.W. "Polyethylene." Polymer Toughening. Ed. Arends, C.B. Marcel Dekker, Inc.: New York, 1996, pp. 189-235.